Dimensioning and Power Management of Hybrid Energy Storage Systems for Electric Vehicles With Multiple Optimization Criteria

Huilong Yu, *Member, IEEE*, Francesco Castelli-Dezza, *Member, IEEE*, Federico Cheli, *Member, IEEE*, Xiaolin Tang, *Member, IEEE*, Xiaosong Hu, *Senior Member, IEEE*, and Xianke Lin

***Abstract*—Hybrid energy storage systems (HESS) that combine lithium-ion batteries and supercapacitors are considered as an attractive solution to overcome the drawbacks of battery-only energy storage systems, such as high cost, low power density, and short cycle life, which hinder the popularity of electric vehicles. A properly sized HESS and an implementable real-time power management system are of great importance to achieve satisfactory driving mileage and battery cycle life. However, dimensioning and power management problems are quite complicated and challenging in practice. To address these challenges, this article proposes a bilevel multiobjective design and control framework with the nondominated sorting genetic algorithm NSGA-II and fuzzy logic control (FLC) as key components, to obtain an optimal sized HESS and the corresponding optimal real-time power management system based on FLC simultaneously. In particular, a vectorized fuzzy inference system is devised, which allows large-scale fuzzy logic controllers to run in parallel, thereby improving optimization efficiency. Pareto optimal results of different HESSs incorporating both optimal design and control parameters are obtained efficiently thanks to the vectorization. An example solution chosen from the Pareto front shows that the proposed method can achieve a competitive number of covered laps while improving the battery cycle life significantly.**

***Index Terms*—Electric vehicles (EVs), hybrid energy storage system (HESS), lithium-ion battery, multiobjective power management, supercapacitor (SC), vectorized fuzzy interface.**

Manuscript received February 12, 2020; revised August 18, 2020; accepted October 6, 2020. Date of publication October 13, 2020; date of current version January 22, 2021. This work was supported in part by the National Natural Science Foundation of China under Grants 51875054 and 51705044 and in part by the Chongqing Natural Science Foundation for Distinguished Young Scholars under Grant cstc2019jcyjjq0010, and in part by the Chongqing Science and Technology Bureau, China. Recommended for publication by Associate Editor R. (GE) Zane. *(Corresponding authors: Xiaolin Tang; Xiaosong Hu.)*

Huilong Yu was with the Department of Mechanical Engineering, Politecnico di Milano, Milano 20156, Italy. He is now with the University of Waterloo, Waterloo, ON N2L 3G1, Canada (e-mail: huilong.yu@uwaterloo.ca).

Francesco Castelli-Dezza and Federico Cheli are with the Department of Mechanical Engineering, Politecnico di Milano, 20156 Milano, Italy (e-mail: francesco.castellidezza@polimi.it; federico.cheli@polimi.it).

Xiaolin Tang and Xiaosong Hu are with the State Key Laboratory of Mechanical Transmissions and the Department of Automotive Engineering, Chongqing University, Chongqing 400044, China (e-mail: tangxl0923@cqu.edu.cn; xiaosonghu@ieee.org).

Xianke Lin is with the Department of Automotive, Mechanical and Manufacturing Engineering at the Ontario Tech University, Oshawa, ON L1G 0C5, Canada (e-mail: xiankelin@ieee.org).

Color versions of one or more of the figures in this article are available online at https://ieeexplore.ieee.org.

Digital Object Identifier 10.1109/TPEL.2020.3030822

NOMENCLATURE

N_{bat}	Number of battery cells
η_{AD}	Efficiency of the dc/ac converter
η_{dc}	Efficiency of the dc/dc converter
A	Battery voltage amplitude (V)
A_h	Ah-throughput of the battery
A_{cl}	Pre-exponential factor of battery cycle life model
B	Time constant inverse of the exponential zone (Ah^{-1})
C_{sct}	Total capacity of the supercapacitor pack
E_0	Battery voltage constant (V)
i	Battery current (A)
K	Battery polarization resistance (Ω)
m_{HESS}	Total mass of the HESS (kg)
N_{sc}	Total number of the banks
P_{reqbat}	Net requested power from the battery (kW)
P_{reqsc}	Demand power from the supercapacitor pack (kW)
P_{sc}	Actual total output power of one supercapacitor (kW)
$Q_{\max}$	Battery total capacity (Ah)
R_{bat}	Battery internal resistance (Ω)
R_{cl}	Gas constant
R_{sct}	Total equivalent series resistance of the supercapacitor pack (Ω)
R_{sc}	Series resistance of one supercapacitor (Ω)
T	The absolute temperature
V_c	Open circuit voltage of one supercapacitor (V)
V_{bat}	Battery voltage (V)
V_{ctmax}	The initial open circuit voltage (V)
V_{ct}	Total open circuit voltage of the supercapacitor pack (V)
x_{SOE}	State of energy

I. INTRODUCTION

CHALLENGES of air pollution, fossil oil crisis, and greenhouse gas emissions have attracted unprecedented attention from governments, academia, and industries around the world on electric vehicles (EVs). After rapid development over the past decade, the worldwide promotion and application of EVs have reached a considerable scale. However, the dynamic performance, cost, and durability of EVs are still closely related to the design, integration, and control of the energy storage systems (ESSs) [1]. The high cost and short cycle life of battery-only ESSs have become one of the biggest obstacles to the further penetration of the EVs [2].

Lithium-ion battery-only ESSs with high energy density have become the dominant choices for powering EVs. However, battery degradation can be accelerated when high discharging/charging power demands are required during operation [3], [4]. In contrast, supercapacitors (SCs) can tolerate much more charging/discharging cycles and exhibit superior ability to cope with high power demands due to their special energy storage mechanisms. However, their low energy density hinders their large-scale application in EVs [5]. A hybrid energy storage system (HESS) that combines both lithium-ion batteries and SCs is considered as one of the most promising solutions to solve the abovementioned problems in the battery-only or SC-only energy systems [6], [7]. Existing research has demonstrated that HESSs can dramatically improve the braking energy recuperation efficiency, eliminate the need for battery oversizing, and reduce the weight and cost of the entire system [8]. However, the application of HESS involves complicated sizing and power management problems [9]. The following three paragraphs will review this topic in terms of HESS sizing, power management, and combined sizing and power management.

Both heuristics and gradient-based optimization methods are used in the sizing of HESS. A sample-based global Dividing RECTangles (DIRECT) optimization algorithm is implemented to solve a multiobjective sizing problem of the HESS, and a rule-based power-split control strategy was implemented to evaluate all design solutions in [10]. The Pareto front of energy storage size and fuel economy based on the Bandwidth control strategy was obtained using GA in [11]. Nondominated sorting GA II (NSGA-II) was applied to obtain the Pareto front of battery degradation, mass, and total cost of HESSs in [12] and [13], with predesigned power management algorithms. Hu *et al.* [14] proposed the usage of a convex optimization algorithm to solve the sizing problem of different HESSs, where the size and power control strategy are optimized simultaneously offline.

Rule-based and optimization-based approaches are comprehensively studied in the previous work for the power management problems of HESS [15]. Dusmez and Khaligh [16] and Zhang and Li [17] developed power management strategies for a HESS based on the fuzzy logic control (FLC) and filtering algorithms. Hu *et al.*[18] devised an enhanced frequency diving coordinated control strategy to realize dynamic power regulation of a HESS, Blanes *et al.* [19] also designed a control strategy to let the battery supply low-frequency current demand and the SCs supply the high-frequency part. Veneri *et al.*[20] designed and compared rule-based energy management systems (EMSs) for a HESS. The real-time performance of rule-based EMSs is appealing but its optimality can not be guaranteed. For this reason, gradient-based optimization approaches are widely studied, a real-time utility function-based control for a semiactive HESS was proposed in [21] and the formulated problem was solved based on the Karush–Kuhn–Tucker conditions, and similar work can also be found in [22] and [23]. Model predictive control was utilized also for the power management of HESSs to realize online optimization [24], [25]. There are also other gradient-free optimization approaches developed, for instance, [26] developed a real-time predictive power management strategy based on neural networks and particle swarm optimization algorithm. While a real-time GA-based power management strategy was proposed in [27].

Most of the aforementioned work was focused on either sizing or power management, in which case, only the suboptimal solution was obtained due to the reduced searching space. To this end, some researchers combined these two problems and tried to optimize the sizing parameters and control law parameters simultaneously. The combined sizing and power management problem was formulated as a nonlinear programming problem and solved by an open source nonlinear programming solver IPOPT in [28] and [29]. A similar approach can also be found in [14], where the sizing and power management problem was formulated as an integrated convex optimization problem and solved by CVX. Song *et al.* [30] formulated and solved the sizing and power management problem of a HESS offline based on the Pontryagin's maximum principle. The above reviewed combined approaches are offline, which are quite useful as the reference when design EMSs but not appropriate for real-time implementation. A few studies investigated the combined sizing and real-time power management optimization problem [31], [32]. However, the developed real-time algorithms were either too simple or only single-objective.

In summary, the sizing and control of a HESS should consider multiple objectives, including its lifespan, energy efficiency, and capacity. Combined sizing and power management can help maximize the searching space for better optimality. Besides, parametric real-time EMS design is essential for further optimization and practical application. FLC is real-time, adaptive, and intelligent, it allows different operators to merge nonlinearities and uncertainties in the best way and incorporate heuristic control in the form of If–Then rules. Its effectiveness and distinct advantages in power management of HESS have been demonstrated, especially after optimizing its membership functions (MFs) [32], [33]. However, the optimization of these MFs usually causes low computation efficiency, especially when the designed FLC is complicated.

The primary goal of this article is to develop an efficient multiobjective optimal sizing and real-time power management algorithm for a HESS. The contributions that distinct this article from the previous efforts are as follows. Firstly, a systematic bilevel multiobjective optimal sizing and control framework incorporating the battery dynamic model, SC model, evaluation model, and adaptive parametric real-time EMS is proposed. Secondly, a parametric vectorized fuzzy inference system (VFIS) is devised for the first time to the best of our knowledge, which allows a large number of fuzzy logic controllers running in parallel and enables fast training and optimization. Thirdly, Pareto optimal solutions of a HESS for an electric race car are obtained using NSGA-II under the proposed framework. The corresponding optimal sizing parameters and MFs of a real-time fuzzy logic-based EMS are obtained simultaneously.

Sizing and control of the HESS for an electric race car are investigated as a case study in this article, which aims to minimize the operating cost for a racing team and to reduce the environmental impact caused by the waste battery. The remainder of this article is divided into six parts. Section II elaborates on the proposed bilevel optimal design and power management framework, then presents the formulation of the sizing and power management problem. Section III describes the battery and SC models. Section IV gives the details of the devised FLC based on the vectorized fuzzy inference engine. In

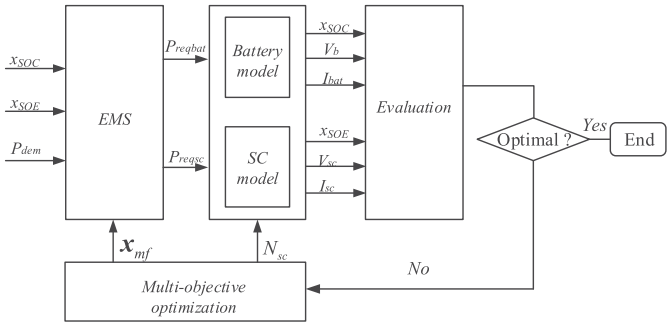

Fig. 1. Framework of the bilevel optimal design and control.

Section V, the simulation parameters and settings are presented in detail. Section VI discusses the obtained results. Finally, Section VII concludes this article.

II. Bilevel Optimal Design and Control Framework

The proposed bilevel optimal design and control framework is presented in Fig. 1. The term "bilevel" here means that the optimization is carried out at both the system integration and controller design levels. The power demand of the driving profile P_{dem}, the battery state of charge x_{SOC}, and SC state of energy x_{SOE} are the inputs of the FLC-based EMS, while the output of the FLC is the requested power from the SC P_{reqsc}, and requested power from the battery is calculated by $P_{\text{reqbat}} = P_{\text{dem}} - P_{\text{reqsc}}$. The outputs of the EMS are the inputs of the battery and SC modeled in Section III, and the evaluation indexes can be calculated based on the outputs of the battery and SC model.

The workflow of the bilevel optimal design and control is illustrated as follows. First, the multiobjective algorithm will generate the sizing parameter matrix and the corresponding static tuning parameter matrix of the power management system. In this article, the matrices represent the number of SC banks and the parameters of the MFs, respectively, in different pages of the optimization parameters. Second, the FLC-based EMS using the new MFs will control the generated HESS to output the demanded power from the battery and SC, respectively. Then, the maximum number of laps can be obtained when both the battery and SC reach the minimum state of charge values set in the constraints, and the capacity loss of the battery is evaluated based on the average current of the battery during the whole process. Many existing studies have proposed models for capacity loss of lithium-ion batteries. Most existing capacity loss models are validated by discharging the battery at a constant current *C* rate, and we have not found any experimentally validated models that can predict the battery capacity loss dynamically. Therefore, we choose to estimate the capacity loss of the battery based on the average load like many previous researchers did, and a statistical histogram discharge *C* rate based approach to evaluate the influences of different *C* rates on the battery cycle life has also been investigated. When the Pareto-front of the two evaluation indexes is obtained, the above iteration will terminate; otherwise, it will continue.

The goal of this study is to find the optimal sizing parameter N_{sc} and the parameter vector $\boldsymbol{x}_{\text{mf}}$ of the MFs, which are the key parameters of the HESS design and real-time FLC-based EMS, respectively. The optimized EMS will output the requested

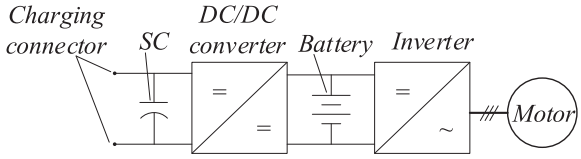

Fig. 2. HESS configuration for an electric race car.

control command series $\mathbf{u}(t) = [P_{\text{reqbat}}, P_{\text{reqsc}}]$ to maximize the number of traveled laps J_{laps} and battery cycle life J_{lifebat} on a given race circuit

$$\max J = [J_{\text{laps}}(\mathbf{x}(t), \mathbf{u}(t), \mathbf{p}), J_{\text{lifebat}}(\mathbf{x}(t), \mathbf{u}(t), \mathbf{p})] \tag{1}$$

subject to

the first-order dynamic constraints

$$\dot{\mathbf{x}}(t) = \boldsymbol{f}[\mathbf{x}(t), \mathbf{u}(t), t, \mathbf{p}] \tag{2}$$

the boundaries of the state, control, and design variables

$$\begin{aligned} \mathbf{x}_{\min} \le \mathbf{x}(t) \le \mathbf{x}_{\max} \\ \mathbf{u}_{\min} \le \mathbf{u}(t) \le \mathbf{u}_{\max} \\ \mathbf{p}_{\min} \le \mathbf{p} \le \mathbf{p}_{\max} \end{aligned} \tag{3}$$

the algebraic path constraints

$$\boldsymbol{g}_{\min} \le \boldsymbol{g}[\mathbf{x}(t), \mathbf{u}(t), t, \mathbf{p}] \le \boldsymbol{g}_{\max} \tag{4}$$

and the boundary conditions

$$\boldsymbol{b}_{\min} \le \boldsymbol{b}[\mathbf{x}(t_0), t_0, \mathbf{x}(t_f), t_f, \mathbf{p}] \le \boldsymbol{b}_{\max} \tag{5}$$

where $\dot{\boldsymbol{x}}$ is the first-order derivative of the state variables, $\boldsymbol{f}$ is the dynamic model, $\mathbf{x}$, $\mathbf{u}$, and $\mathbf{p}$ are the state, control, and design vector, respectively, and their lower and upper bounds are $\mathbf{x}_{\min}$, $\mathbf{u}_{\min}$, $\mathbf{p}_{\min}$ and $\mathbf{x}_{\max}$, $\mathbf{u}_{\max}$, $\mathbf{p}_{\max}$, respectively. While $\boldsymbol{g}$ and $\boldsymbol{b}$ are the path and boundary equations, respectively, with their lower and upper bounds $\boldsymbol{g}_{\min}$, $\boldsymbol{b}_{\min}$ and $\boldsymbol{g}_{\max}$, $\boldsymbol{b}_{\max}$.

In this article, the algebraic path constraint $\boldsymbol{g}$ is eliminated by introducing a simple relaxation in (12), the state variables $\boldsymbol{x}$, control variables $\boldsymbol{u}$, design parameters $\boldsymbol{p}$, and the boundary constraints $\boldsymbol{b}$ will be presented in the following paragraphs.

III. Modeling of the HESS

The HESS configuration for an electric race car is demonstrated in Fig. 2. The SC can output and absorb high peak power by controlling a bidirectional dc/dc converter that interfaces the SC to the dc link of the battery. Moreover, the voltage of SC can be used in a wide range with the help of the dc/dc converter [6]. There is a dc/ac inverter between the dc link and the ac motor, which converts direct current to alternating current. In particular, the dc/ac inverter allows a wide-range input voltage from the dc link. This configuration has a smaller mass, is easier for installation and costs less compared to an active parallel topology.

In this section, the dynamic characteristics of the implemented lithium-ion battery are analyzed first, and a dynamic battery model is employed after comparison. Then, the details of the battery cycle life model are presented. A simplified SC model is illustrated at the end of this section.

A. Dynamic Battery Model

The battery models for simulating the battery behavior basically include the semiempirical, electrochemical, and electrical ones [34], [35]. The widely used one is the effective internal resistance (Rint) model, where the voltage and resistance are described as functions of SOC based on experimental data. However, this model with only SOC as an independent variable can not capture the influences of the *C* rate and SOC simultaneously. In order to obtain the optimal sizing parameters and power management strategy for the HESS considering the characteristics of the battery in practical conditions, it is necessary to implement a proper battery model that can describe the battery dynamic behavior precisely. In this article, a modified Shepherd model is employed to depict the dynamic characteristics of the battery during the charging and discharging process [36]. The dynamic battery model is represented by (6) and (7) with the assumption that the internal resistance is constant and the thermal behavior of the battery is neglected. The Coulombic efficiency is kind of taken into account with the terms multiplied by the polarization resistance since there is always voltage drop when the discharge current is not zero.

Discharge

$$V_{\text{bat}} = E_0 - \frac{KQ_{\max}}{Q_{\max} - it}it - \frac{KQ_{\max}}{Q_{\max} - it}i - R_{\text{bat}}i + Ae^{(-B\cdot it)} \tag{6}$$

Charge

$$V_{\text{bat}} = E_0 - \frac{KQ_{\max}}{Q_{\max} - it}it - \frac{KQ_{\max}}{it - 0.1Q_{\max}}i - R_{\text{bat}}i + Ae^{(-B\cdot it)} \tag{7}$$

where V_{bat} is the battery voltage (V), E_0 is the voltage constant (V), K is the polarization constant or polarization resistance, $Q_{\max}$ is the total capacity, i is the battery current, and R_{bat} is the internal resistance. The battery discharge $(i > 0)$ or charge $(i < 0)$ it is denoted as

$$it = \int idt. \tag{8}$$

The calculation of the voltage amplitude $A\,(V)$, time constant inverse B (Ah^{-1}) of the exponential zone, the polarization resistance K (Ω), and the voltage constant E_0 (V) in (6) and (7) are referred to [36]. The battery model is calibrated with experimental data, the comparison of the fitted model and the real data is demonstrated as Fig. 3. The fitted semiempirical model can represent the real battery dynamics satisfactorily.

The state of charge of the battery x_{soc} and its derivative $\dot{x}_{\text{soc}}$ is denoted as (9) and (10), respectively.

$$x_{\text{soc}} = 100\left(1 - \frac{1}{3600Q_{\max}}\int_0^{t_f} idt\right) \tag{9}$$

$$\dot{x}_{\text{soc}} = -\frac{1}{36Q_{\max}}i. \tag{10}$$

The charging/discharging i is denoted as

$$i = \begin{cases} \dfrac{P_{\text{reqbat}}}{N_{\text{bat}}V_{\text{bat}}\eta_{AD}}, & P_{\text{reqbat}} \geq 0 \\ \dfrac{P_{\text{reqbat}}\eta_{AD}}{N_{\text{bat}}V_{\text{bat}}}, & P_{\text{reqbat}} < 0 \end{cases} \tag{11}$$

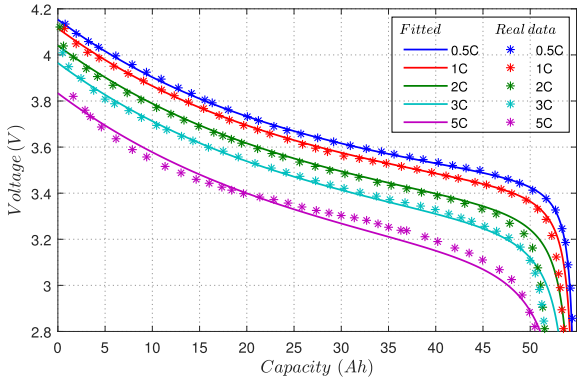

Fig. 3. Comparison of the fitted dynamic battery model and the real data.

where η_{AD} is the efficiency of the dc/ac converter taking into account the motor efficiency as a constant value. In this article, the number of battery cells N_{bat} is determined by the available total mass of the HESS m_{HESS} and the number of the SC banks N_{sc}, as shown in (12). The total mass of the HESS is fixed in this article given the fact that the mass of a race car is strictly limited in general.

$$N_{\text{bat}} = \lfloor (m_{HESS} - N_{\text{sc}}m_{\text{bank}})/m_{\text{cell}} \rfloor. \tag{12}$$

B. Battery Cycle Life Model

In recent years, substantial efforts have been made by both academia and industries to develop models that can predict the degradation of the lithium-ion batteries accurately [37]. Different models were developed to account for various factors responsible for capacity fade such as parasitic side reactions, solid electrolyte interphase formation, and resistance increasing. However, experimental data are essential for studying the aging processes of a battery system and verifying the capacity fading mechanisms. A revised semiempirical model based on the Arrhenius equation was widely used in the optimization and control problems related with batteries [38]. As shown in (13)–(16), the capacity loss of this model is expressed as a function of the discharge current rate C_{rate}, temperature T, and ampere-hour throughout A_h

$$Q_{\text{loss}} = A_{cl}\exp\left(\frac{-E_a}{R_{\text{cl}}}\right)(A_h)^z \tag{13}$$

where Q_{loss} represents the battery capacity loss, A_{cl} the preexponential factor, E_a the activation energy from Arrhenius law (J), R_{cl} is the gas constant of 8.314, T is the absolute temperature (K), and A_h is the Ah-throughput, which represents the amount of charge delivered by the battery during cycling.

The preexponential factor A in (13) is proved to be sensitive to the discharge current rate C_{rate} in the experiments [39], and it is fitted using [40, (14)]

$$\ln A_{\text{cl}} = a\cdot\exp(-b\cdot C_{\text{rate}}) + c. \tag{14}$$

The activation energy can be fitted as a linear function of discharge current rate [39]

$$E_a = d + e\cdot C_{\text{rate}} \tag{15}$$

where a, b, c, d, and e are the correction parameters of the battery cycle life model.

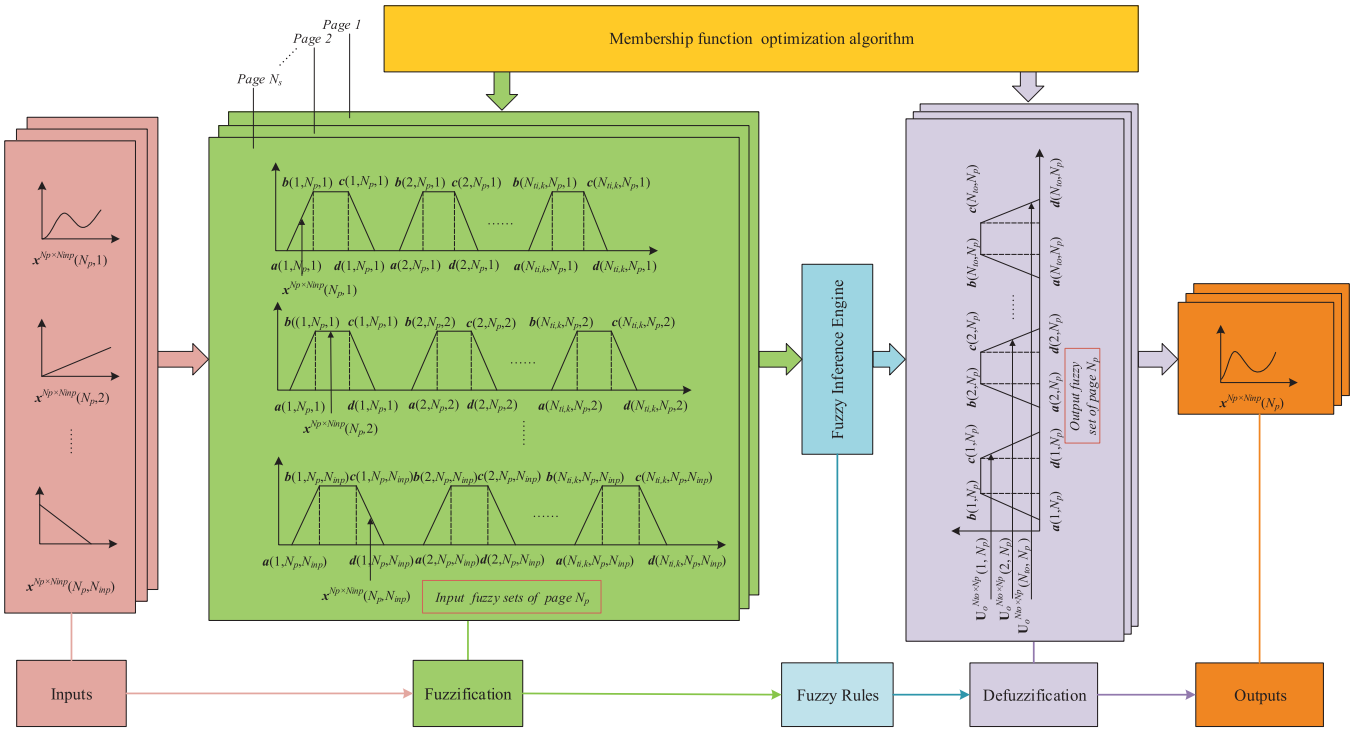

Fig. 4. Framework of the vectorized FLC. The developed VFIS is capable of handling $N_p \times N_{\text{inp}}$ dimensional inputs with N_p pages of MFs each time, which means that N_p fuzzy controllers (can be hundreds of thousands depending on the performance of the utilized CPUs) can work at the same time with the same page number of inputs and outputs.

The Ah-throughput can be expressed as

$$A_h = \int_0^{t_f} \frac{i}{3600} dt \tag{16}$$

where i is the discharge current, t_f is the end time of the current profile.

In addition to using the average current rate to evaluate the capacity loss, a statistical method [10] was also implemented to estimate the effect of nonuniform current rate on battery cycle life.

C. SC Model

In this article, the capacity fading of the SC is neglected because it has much longer cycle life than lithium-ion batteries. The SC model is simplified to a series connection of a resistance and a SC bank [5]. Also, the efficiency of the dc/dc converter between the SC and the dc link is assumed to be a constant value of 0.95. The recursive SC model is derived as follows:

$$\dot{V}_{\text{ct}} = \begin{cases} -\dfrac{V_{\text{ct}} - \sqrt{V_{\text{ct}}^2 - 4R_{\text{sct}}P_{\text{reqsc}}/(\eta_{\text{AD}}\eta_{\text{dc}})}}{2C_{\text{sct}}R_{\text{sct}}} & P_{\text{reqsc}} \geq 0 \\ -\dfrac{V_{\text{ct}} - \sqrt{V_{\text{ct}}^2 - 4R_{\text{sct}}P_{\text{reqsc}}\eta_{\text{AD}}\eta_{\text{dc}}}}{2C_{\text{sct}}R_{\text{sct}}} & P_{\text{reqsc}} < 0 \end{cases} \tag{17}$$

$$x_{\text{SOE}} = \frac{{V_{\text{ct}}}^2}{V_{\text{ctmax}}^2} \tag{18}$$

where $V_{\text{ct}} = V_c N_{\text{sc}}$ is the total open-circuit voltage of the SC pack assuming that all banks have a uniform behavior, t_{k+1} is the time at step $k+1$, $R_{\text{sct}} = N_{\text{sc}}R_{\text{sc}}$ is the total equivalent series resistance, P_{reqsc} is the demand power from the SC, η_{dc} is the efficiency of the dc/dc converter, $C_{\text{sct}} = C_{\text{bank}}/N_{\text{sc}}$ is the total capacity, x_{SOE} is the state of energy, V_{ctmax} is the initial open circuit voltage, V_c is the open circuit voltage of one SC, N_{sc} is the total number of the banks, and R_{sc} is the series resistance of one SC.

The actual total output power of the SC pack is calculated as

$$P_{\text{sc}} = V_{\text{ct}} \cdot \frac{V_{\text{ct}} - \sqrt{V_{\text{ct}}^2 - 4R_{\text{sct}}P_{\text{reqsc}}/\eta_{\text{AD}}\eta_{\text{dc}}}}{2R_{\text{sct}}}. \tag{19}$$

IV. FLC With Vectorized Fuzzy Inference Engine

The proposed FLC in this section consists of If–Then fuzzy rules, fuzzification, fuzzy inference engine, and defuzzification modules. To speed up the optimization and take advantage of the powerful matrix processing capability of MATLAB, a VFIS shown in Fig. 4 is developed for the first time according to the state-of-the-art literature. The following paragraph will present the details of fuzzy rules, MFs, vectorized fuzzification, fuzzy inference engine, and defuzzification operations of the developed vectorized FLC.

A. Fuzzy Rules

Fuzzy rules are a set of If–Then linguistic rules used to formulate the conditional relationships that compose a fuzzy logic controller. For instance, a fuzzy rule can be: if SOC is *high* and SOE is *high*; and if P_{req} is *positive high* then P_{sc} is *positive big*. It is reasonable to devise the same If–Then rules

for the control of HESSs with different sizes, since the control objectives of all the HESSs are the same in this article. The developed fuzzy rules are demonstrated as Fig. 6(a), where the labels N, P, S, M, and B mean negative, positive, small, medium, and big, respectively. The basic idea of the fuzzy rule is to utilize the SC as a buffer to reduce the high peak power impact on battery and absorb more regenerative braking power.

B. Membership Functions

The concept of MFs was introduced by Zadeh in the first paper on fuzzy sets [41]. A MF is a curve or a function that defines how each point of the input variables is mapped to a membership value between 0 and 1. It is quite challenging to design the optimal MFs for each HESS manually according to the engineering experiences. Besides, considering that the performance of the FLCs is sensitive to their MFs, different MFs of the FLCs with the same fuzzy rules should be devised for different sizes of HESS. Based on these considerations, the parameters of the MFs are selected as parts of the parameters to be optimized in this article. The trapezoidal-shaped MF is selected for the fuzzy inference engine based on the considerations that it has high flexibility [9].

C. Vectorized Fuzzification

During the fuzzification stage, the input variables are identified to the fuzzy sets (MFs) they belong to and the respective degree of membership to each relevance will be assigned. For a FIS with trapezoidal-shaped MFs and a number of N_{inp} inputs, the fuzzy sets of each can be described using a matrix $\boldsymbol{S}_k = [\boldsymbol{a}_k, \boldsymbol{b}_k, \boldsymbol{c}_k, \boldsymbol{d}_k] \in \mathcal{R}^{N_p \times N_{ti,k} \times 4}$. N_p is the total page number of the inputs; $N_{ti,k}$ is the number of fuzzy linguistic sets of state input k, $k \in \{1, 2, ..., N_{\text{inp}}\}$ and $a,\ b,\ c,\ d$ are the variables that define one trapezoid. The input matrix is denoted as $\mathbf{x}_k \in \mathcal{R}^{N_p}$, for $\mathbf{X}_k$, its membership matrix $\boldsymbol{\mu}_k \in \mathcal{R}^{N_p \times N_{ti,k}}$ can be denoted as

$$\begin{cases} \boldsymbol{\mu}_k(\boldsymbol{a}_k \le \mathbf{X}_k < \boldsymbol{b}_k) = \dfrac{\mathbf{X}_k - \boldsymbol{a}_k}{\boldsymbol{b}_k - \boldsymbol{a}_k} \\ \boldsymbol{\mu}_k(\boldsymbol{b}_k \le \mathbf{X}_k \le \boldsymbol{c}_k) = \boldsymbol{I} \\ \boldsymbol{\mu}_k(\boldsymbol{c}_k < \mathbf{X}_k \le \boldsymbol{d}_k) = \dfrac{\boldsymbol{d}_k - \mathbf{X}_k}{\boldsymbol{d}_k - \boldsymbol{c}_k} \end{cases} \tag{20}$$

where $\boldsymbol{a}_k, \boldsymbol{b}_k, \boldsymbol{c}_k, \boldsymbol{d}_k,$ and $\boldsymbol{I}$ belong to $\mathcal{R}^{N_p \times N_{ti,k}}$, and $\mathbf{X}_k$ is denoted as

$$\mathbf{X}_k = [\underbrace{\mathbf{x}_k, \mathbf{x}_k, ..., \mathbf{x}_k}_{N_{ti,k}}] \in \mathcal{R}^{N_p \times N_{ti,k}}. \tag{21}$$

The membership array $\mathbf{U}$ for input $\mathbf{X}$ can be constructed as

$$\mathbf{U} = \{\boldsymbol{\mu}_1, ..., \boldsymbol{\mu}_k, ..., \boldsymbol{\mu}_{N_{inp}}\} \in \mathcal{R}^{N_p \times N_{ti,k} \times N_{inp}} \tag{22}$$

D. Vectorized Fuzzy Inference Engine

Fuzzy inference maps an input space to an output space using fuzzy logic. A FIS tries to formalize the reasoning process of human language by means of fuzzy logic (the built fuzzy If–Then rules). The process of fuzzy inference involves all of the MFs, If–Then rules, linguistic variables of the inputs and outputs. Mamdani's fuzzy inference method is the most commonly used fuzzy methodology. The search-able fuzzy inference engine is able to map only one page of the inputs to one page of the outputs. This section will give an elaborate description of the developed powerful VFIS, which allows a large number of FLCs operating in parallel based on Mamdani's fuzzy inference method.

The linguistic variables are programmed with their integer indexes from the smallest to the biggest in this article. For instance, the fuzzy sets {NB, NM, NS, PS, PM, PB} of the third input in Fig. 6 are mapped to $\{1, 2, ..., N_{ti,k}\}$ correspondingly, here $N_{ti,k} = 6,\ k = 3$. The fuzzy rule matrix $\mathfrak{R} \in \mathcal{R}^{N_r \times (N_{inp} + N_o)}$ is constructed with the mapped integer indexes, N_r is the number of fuzzy rules and N_o is the number of outputs. For instance

$$\begin{array}{rcccc} \text{Rule}: & x_{\text{SOC}} & x_{\text{SOE}} & P_{\text{req}} & P_{\text{sc}} \\ \mathfrak{R}(N_r): & 1 & 3 & 6 & 6 \end{array} \tag{23}$$

where $\mathfrak{R}(N_r)$ denotes the fuzzy rule N_r, it means the rule like if SOC is *low* and SOE is *high* and if P_{req} is *positive high* then P_{sc} is *positive high*. The working scheme of the VFIS is illustrated as follows:

1) Repeatedly copy the membership matrix $\boldsymbol{\mu}_k$ into N_r blocks, and we can obtain

$$\boldsymbol{\mu}_k^{\text{temp}} = [\underbrace{\boldsymbol{\mu}_k; \boldsymbol{\mu}_k; ...; \boldsymbol{\mu}_k}_{N_r}],\ \boldsymbol{\mu}_k^{\text{temp}} \in \mathcal{R}^{N_p \times N_{ti,k} \times N_r}. \tag{24}$$

2) Create index matrix $\mathbf{L}_{in} \in \mathcal{R}^{N_p \times N_{ti,k} \times N_r}$ for input k

$$\mathbf{L}_{in} = \underbrace{\left\{ \begin{bmatrix} 1 & 2 & \cdots & N_{ti,k} \\ 1 & 2 & \ldots & N_{ti,k} \\ \vdots & \vdots & \vdots & \vdots \\ 1 & 2 & \cdots & N_{ti,k} \end{bmatrix}, \cdots \begin{bmatrix} 1 & 2 & \cdots & N_{ti,k} \\ 1 & 2 & \ldots & N_{ti,k} \\ \vdots & \vdots & \vdots & \vdots \\ 1 & 2 & \cdots & N_{ti,k} \end{bmatrix} \right\}}_{N_p} N_r. \tag{25}$$

3) Repeatedly copy the kth column of the rule matrix $\mathfrak{R} \in \mathcal{R}^{N_r \times (N_{\text{inp}} + N_o)}$ into $N_p \times N_{ti,k}$ block arrangement $\mathfrak{R}_{\text{temp}} \in \mathcal{R}^{N_p \times N_{ti,k} \times N_r}$, $k \in \{1, 2, \ldots, N_{\text{inp}}\}$

$$\mathfrak{R}_{\text{temp}} = \underbrace{\left\{ \begin{bmatrix} \mathfrak{R}_k, & \mathfrak{R}_k, & \ldots, & \mathfrak{R}_k \\ \mathfrak{R}_k, & \mathfrak{R}_k, & \ldots, & \mathfrak{R}_k \\ \vdots, & \vdots, & \ldots, & \vdots \\ \mathfrak{R}_k, & \mathfrak{R}_k, & \ldots, & \mathfrak{R}_k \end{bmatrix} \right\}}_{N_{ti,k}} N_p \tag{26}$$

4) Get the effective membership matrix $\boldsymbol{\mu}_{\text{eff},k}$ for input $k \in \{1, 2, \ldots, N_{\text{inp}}\}$

$$\boldsymbol{\mu}_{eff,k} = \boldsymbol{\mu}_k(L_{\text{in}} == \mathfrak{R}_{\text{temp}}), \boldsymbol{\mu}_{\text{eff},k} \in \mathcal{R}^{N_p \times N_{ti,k} \times N_r}. \tag{27}$$

5) Combine and get the final membership matrix $\mathbf{U}_{\text{in}} \in \mathcal{R}^{N_p \times N_r \times N_{inp}}$ for all the input $\mathbf{X}$

$$\mathbf{U}_{\text{in}} = \underbrace{\left\{ \bigcup_{j=1}^{N_{ti,k}} \boldsymbol{\mu}_{\text{eff},k}(j), \bigcup_{j=1}^{N_{ti,k}} \boldsymbol{\mu}_{eff,k}(j), ..., \bigcup_{j=1}^{N_{ti,k}} \boldsymbol{\mu}_{\text{eff},k}(j) \right\}}_{N_{\text{inp}}}. \tag{28}$$

6) Get the mapped membership matrix $\mathbf{U}_o$ for the output fuzzy sets

$$\mathbf{U}_o = \bigcap_{k=1}^{N_{\text{inp}}} \mathbf{U}_{\text{in}}(k), \mathbf{U}_o \in \mathcal{R}^{N_p \times N_r}. \tag{29}$$

7) Create index matrix $L_o \in \mathcal{R}^{N_p \times N_r \times N_{to}}$ for output the fuzzy sets

$$\mathbf{L}_o = \underbrace{\left\{ \begin{bmatrix} 1\ 2 \cdots N_{to} \\ 1\ 2 \ldots N_{to} \\ \vdots\ \vdots\ \vdots\ \ \vdots \\ 1\ 2 \cdots N_{to} \end{bmatrix}, \cdots \begin{bmatrix} 1\ 2 \cdots N_{to} \\ 1\ 2 \ldots N_{to} \\ \vdots\ \vdots\ \vdots\ \ \vdots \\ 1\ 2 \cdots N_{to} \end{bmatrix} \right\}}_{N_p} N_r. \tag{30}$$

8) Repeatedly copy the column of output fuzzy sets in the rule matrix $\mathfrak{R} \in \mathcal{R}^{N_r \times (N_{\text{inp}}+N_o)}$ into a $N_p \times N_{to}$ block arrangement $\mathfrak{R}_{o\text{temp}} \in \mathcal{R}^{N_p \times N_r \times N_{to}}$, N_{to} is the number of fuzzy linguistic sets of output

$$\mathfrak{R}_{o\text{temp}} = \underbrace{\left\{ \begin{bmatrix} \mathfrak{R}_{N_o}, & \mathfrak{R}_{N_o}, & \ldots, & \mathfrak{R}_{N_o} \\ \mathfrak{R}_{N_o}, & \mathfrak{R}_{N_o}, & \ldots, & \mathfrak{R}_{N_o} \\ \vdots, & \vdots, & \ldots, & \vdots \\ \mathfrak{R}_{N_o}, & \mathfrak{R}_{N_o}, & \ldots, & \mathfrak{R}_{N_o} \end{bmatrix} \right\}}_{N_{\text{to}}} N_p. \tag{31}$$

9) Repeatedly copy the membership matrix of the output fuzzy sets $\mathbf{U}_o \in \mathcal{R}^{N_p \times N_r}$ into N_{to} blocks $\mathbf{U}_{o,\text{temp}}$:

$$\mathbf{U}_{o,\text{temp}} = \underbrace{\{\mathbf{U}_o, \mathbf{U}_o, ..., \mathbf{U}_o\}}_{N_{\text{to}}}, \mathbf{U}_{o,\text{temp}} \in \mathcal{R}^{N_p \times N_r \times N_{\text{to}}} \tag{32}$$

10) Get the effective membership matrix $\mathbf{U}_{\text{eff},o}$ of all the output fuzzy sets

$$\mathbf{U}_{\text{eff},o} = \mathbf{U}_{o,\text{temp}}(L_o == \mathfrak{R}_{o\text{temp}}), \mathbf{U}_{\text{eff},o} \in \mathcal{R}^{N_p \times N_r \times N_{\text{to}}} \tag{33}$$

11) Merge the membership matrix of the output fuzzy sets in all the fuzzy rules

$$\mathbf{U}_{o,\text{final}} = \bigcup_{i=1}^{N_r} \mathbf{U}_{o,\text{eff}}(i), \mathbf{U}_{o,\text{final}} \in \mathcal{R}^{N_p \times N_{\text{to}}}. \tag{34}$$

By the above calculation, the membership of each trapezoid of the output fuzzy set is obtained as $\mathbf{U}_{o,final}$, and the next step is the defuzzification.

E. Vectorized Defuzzification

The purpose of the defuzzification process is to produce a quantifiable result in crisp logic based on the given fuzzy sets and corresponding membership degrees. The defuzzification process based on the center of gravity method is demonstrated in Fig. 5.

The procedure is elaborated as following.

1) Discrete the output fuzzy sets into N_{dis} parts $\boldsymbol{x}_o \in \mathcal{R}^{N_{\text{dis}}}$ from its minimum value $\boldsymbol{x}_{o,\min}$ to the maximum one $\boldsymbol{x}_{o,\max}$

$$\boldsymbol{x}_o = [\boldsymbol{x}_{o,\min} : (\boldsymbol{x}_{o,\max} - \boldsymbol{x}_{o,\min})\ (N_{dis} - 1) : \boldsymbol{x}_{o,\max}] \tag{35}$$

where the value of N_{dis} affects the accuracy of the crisp output, for instance, the increasing of N_{dis} will improve the precision but will increase the computational burden.

2) Repeatedly copy $\boldsymbol{x}_o \in \mathcal{R}^{N_{\text{dis}}}$ and output fuzzy set $\boldsymbol{S}_o = [\boldsymbol{a}_o, \boldsymbol{b}_o, \boldsymbol{c}_o, \boldsymbol{d}_o] \in \mathcal{R}^{N_{to} \times N_p \times 4}$, we can obtain $\boldsymbol{x}_{o,\text{temp}} \in \mathcal{R}^{N_{\text{to}} \times N_p \times N_{\text{dis}}}$ and $\boldsymbol{S}_{o,\text{temp}} \in \mathcal{R}^{N_{\text{to}} \times N_p \times N_{\text{dis}}}$, respectively, as

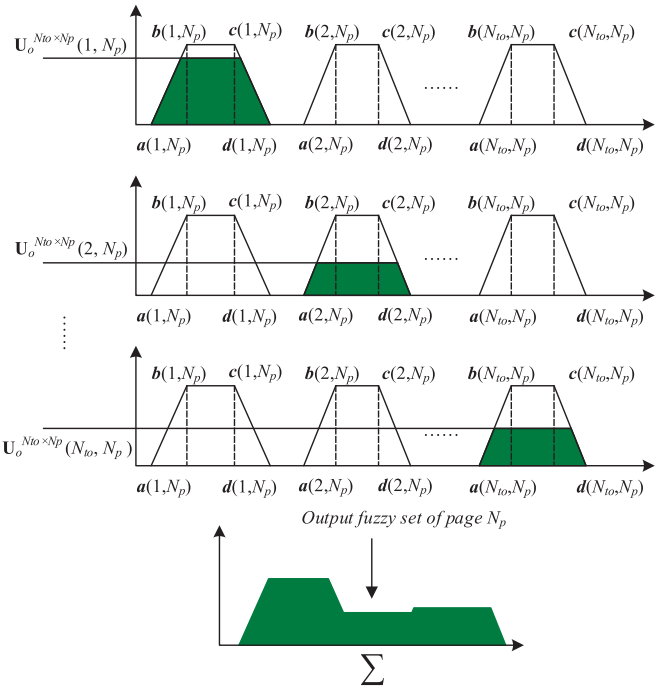

Fig. 5. Defuzzification process based on the center of gravity method.

$$\boldsymbol{x}_{o,\text{temp}} = \underbrace{\left\{ \begin{bmatrix} \boldsymbol{x}_o, & \boldsymbol{x}_o, & \ldots, & \boldsymbol{x}_o \\ \boldsymbol{x}_o, & \boldsymbol{x}_o, & \ldots, & \boldsymbol{x}_o \\ \vdots, & \vdots, & \ldots, & \vdots \\ \boldsymbol{x}_o, & \boldsymbol{x}_o, & \ldots, & \boldsymbol{x}_o \end{bmatrix} \right\}}_{N_{\text{to}}} N_p \tag{36}$$

$$\boldsymbol{S}_{o,\text{temp}} = \underbrace{[\boldsymbol{S}_o, \boldsymbol{S}_o, ..., \boldsymbol{S}_o]}_{N_{\text{dis}}}. \tag{37}$$

3) Calculate the membership matrix of $\boldsymbol{x}_{o,\text{temp}}$ based on the output fuzzy set $\boldsymbol{S}_{o,\text{temp}} = [\boldsymbol{a}_{o,\text{temp}}, \boldsymbol{b}_{o,\text{temp}}, \boldsymbol{c}_{o,\text{temp}}, \boldsymbol{d}_{o,\text{temp}}] \in \mathcal{R}^{N_{\text{to}} \times N_p \times N_{\text{dis}} \times 4}$

$$\begin{cases} \boldsymbol{\mu}_o(\boldsymbol{a}_{o,\text{temp}} \le \boldsymbol{x}_{o,\text{temp}} < \boldsymbol{b}_{o,\text{temp}}) = \dfrac{\boldsymbol{x}_{o,\text{temp}} - \boldsymbol{a}_{o,\text{temp}}}{\boldsymbol{b}_{o,\text{temp}} - \boldsymbol{a}_{o,\text{temp}}} \\ \boldsymbol{\mu}_{o,\text{temp}}(\boldsymbol{b}_{o,\text{temp}} \le \boldsymbol{x}_{o,\text{temp}} \le \boldsymbol{c}_{o,\text{temp}}) = \boldsymbol{I} \\ \boldsymbol{\mu}_o(\boldsymbol{c}_{o,\text{temp}} < \boldsymbol{x}_{o,\text{temp}} \le \boldsymbol{d}_{o,\text{temp}}) = \dfrac{\boldsymbol{d}_{o,\text{temp}} - \boldsymbol{x}_{o,\text{temp}}}{\boldsymbol{d}_{o,\text{temp}} - \boldsymbol{c}_{o,\text{temp}}} \end{cases} \tag{38}$$

4) Repeatedly copy the membership matrix $\mathbf{U}_{o,\text{final}}$ in to N_{dis} blocks $\mathbf{U}_{o,\text{temp}} \in \mathcal{R}^{N_{\text{to}} \times N_p \times N_{\text{dis}}}$

$$\mathbf{U}_{o,\text{temp}} = \underbrace{[\mathbf{U}_{o,\text{final}}, \mathbf{U}_{o,\text{final}}, ..., \mathbf{U}_{o,\text{final}}]}_{N_{\text{dis}}} \tag{39}$$

5) Find the effective membership matrix

$$\mathbf{U}_{\text{eff},o} = \mathbf{U}_{o,\text{temp}} \bigcap \boldsymbol{\mu}_o, \mathbf{U}_{\text{eff},o} \in \mathcal{R}^{N_{\text{to}} \times N_p \times N_{\text{dis}}} \tag{40}$$

6) Merge the membership matrix obtained in last step

$$\mathbf{U}_{o,x} = \bigcup_{i=1}^{N_r} \mathbf{U}_{\text{eff},o}(i), \mathbf{U}_{o,x} \in \mathcal{R}^{N_p \times N_{\text{dis}}} \tag{41}$$

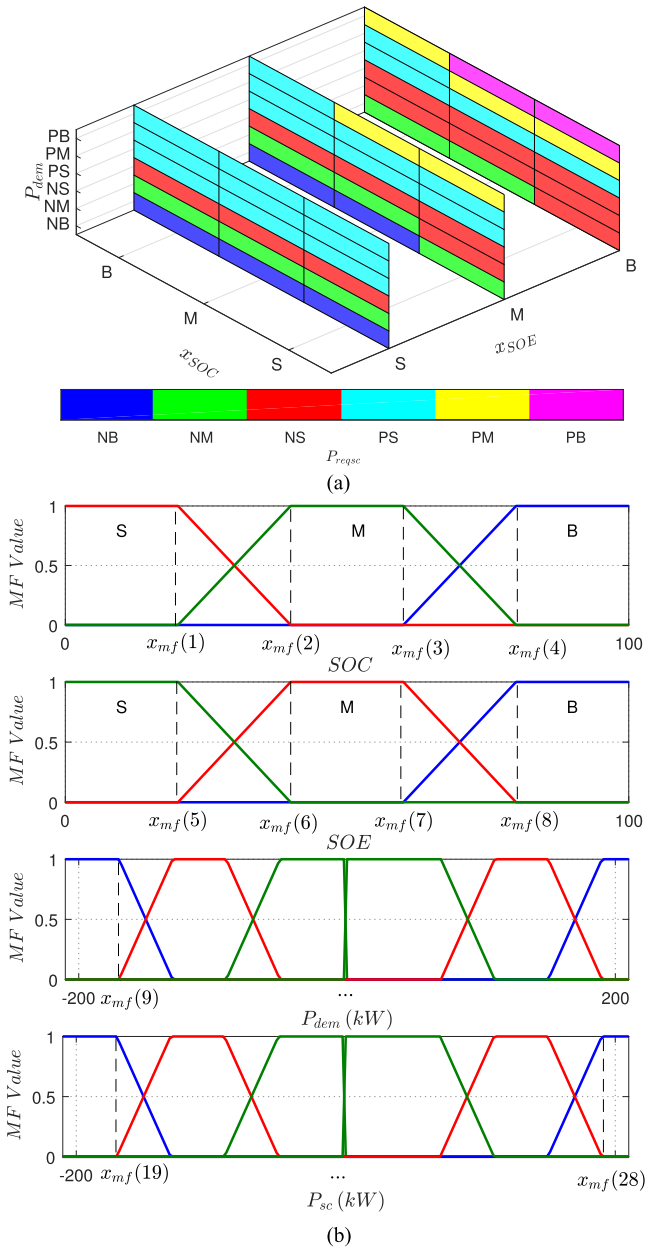

Fig. 6. Parameters of the FLC based EMS. (a) Fuzzy rules of the EMS. (b) MF design parameters of the EMS.

7) Calculate the crisp output matrix for all the input matrices

$$y = \frac{\sum_{i=1}^{N_{\text{dis}}} \boldsymbol{x}_o(i) \circ \mathbf{U}_{o,x}\left(\boldsymbol{x}_o(i)\right)}{\sum_{i=1}^{N_{\text{dis}}} \mathbf{U}_{o,x}\left(\boldsymbol{x}_o(i)\right)}, y \in \mathcal{R}^{N_p}. \tag{42}$$

In order to design the fuzzy rules and MFs conveniently, the devised vectorized FLC modules illustrated above are developed in MATLAB with standard and user-friendly interfaces.

V. Simulation Parameters and Settings

The state variables include the battery state of charge x_{SOC} and state of energy of the SCs x_{SOE}, $\mathbf{x} = [x_{SOC},\ x_{SOE}]$. The control variable output by the FLC in this article is the requested power from the SCs $\mathbf{u} = P_{\text{reqsc}}$, while the demand power from

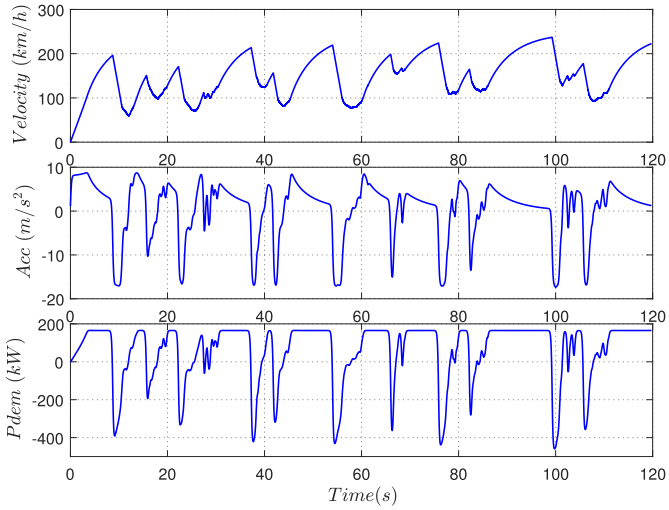

Fig. 7. Power demand in Nurburgring circuit.

the battery can be calculated by $P_{\text{reqbat}} = P_{\text{dem}} - P_{\text{reqsc}}$. In addition, only SCs are used for regenerative braking in order to improve the battery cycle life. The design parameter vector is $\mathbf{p} = \{N_{\text{sc}}, \boldsymbol{x}_{\text{mf}}\}$. The designed fuzzy rules and initial MFs are demonstrated in Fig. 6, and there are 28 parameters of the devised MFs plus one design parameter of the HESS in one page of parameters to be optimized. The design vector $\mathbf{p}$ is constrained by defining $\mathbf{p}_{\min}$ and $\mathbf{p}_{\max}$.

The operating profile of an electric race car is quite different from the one of a conventional EV running on a city road. Thus, standard driving cycles are not suitable for research on electric race cars. The real driving cycle of a race car in the Nurburgring circuit is chosen as the test scenario. he demand driving/braking power is calculated by (43). The corresponding velocity profile, acceleration profile, and demand power are demonstrated as Fig. 7.

$$P_{\text{dem}} = \left(\frac{1}{2}\rho C_d A v^2 + f m_v g + m_v a\right) v. \tag{43}$$

The detailed simulation parameters of the race car, the XALT 53 Ah (rated) high energy lithium-ion battery, the Maxwell Technologies 2.85V/3400 F high-performance SC, and the converters are illustrated in Table I.

In the FLC-based EMS, the SOE, and current of the SC are constrained between 0.1 and 0.99, -2000 A and 2000 A, respectively. While the SOC of the lithium-ion battery is constrained between 0.2 and 0.9, the current is regulated by adjusting the requested power from the battery. When the lithium-ion battery is exhausted, the simulation of one iteration will be terminated and the objective functions will be evaluated. The temperature is for sure very important in any kind of vehicle equipped with batteries, since it can affect the performance of the batteries directly. However, it is very difficult to model the heat generation, dispassion, and the thermal control system of the ESS on an EV precisely. Actually, it is reasonable to assume that the temperature is controlled at a constant value (23 ^oC) by adjusting the thermal control system [1], [42].

TABLE I
PARAMETER VALUES OF THE SIMULATION

Parameters	*Symbol*	*Value*
Vehicle mass (kg)	m_v	570
Aerodynamics coefficient (h^2N/km^2)	$\rho C_d A$	0.075
Rolling resistance coefficient	f	0.016
Mass of the battery cell (kg)	m_{cell}	1.15
Voltage constant of the battery cell (V)	E_0	3.43
Maximum capacity of the battery cell(Ah)	Q_{max}	55
Polarization resistance of the battery cell (Ω)	K	8.85×10^{-5}
Internal resistance of the battery cell (Ω)	R	1.33×10^{-3}
Voltage amplitude of the battery cell (V)	A	0.761
Time constant inverse of the battery cell (Ah^{-1})	B	0.040
Fitting parameter of the pre-exponential factor	a	1.345
Fitting parameter of the pre-exponential factor	b	0.2563
Fitting parameter of the pre-exponential factor	c	9.179
Fitting parameter of activation energy	d	46868
Fitting parameter of activation energy	e	-470.3
Mass of the supercapacitor bank (kg)	m_{bank}	0.52
Supercapacitor bank capacity(F)	C_{bank}	3400
Supercapacitor equivalent series resistance (Ω)	R_s	2.2×10^{-4}
DC/DC converter efficiency	η_{dc}	0.95
DC/AC converter efficiency	η_{AD}	0.96

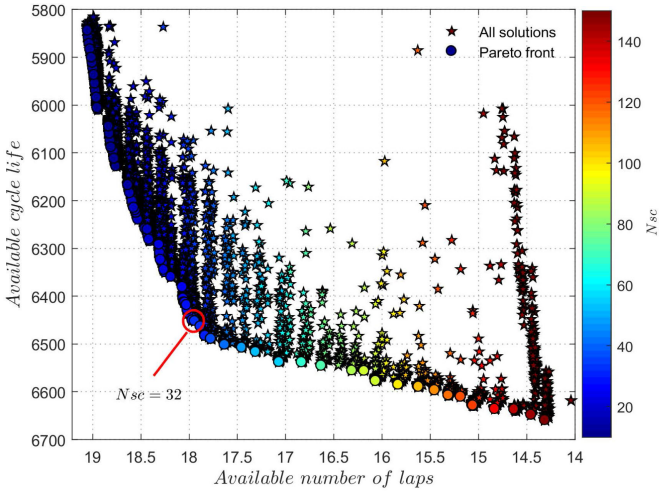

Fig. 8. Multiobjective sizing and control solutions when $m_{\text{HESS}} = 320\,\text{kg}$, each solution is associated with both design and controller parameters.

In this article, a controlled elitist NSGA, which is a variant of NSGA-II [43] is implemented to solve the multiobjective optimization problem. Instead of only choosing the top-ranking nondominated fronts, the controlled elitist GA also favors individuals that can assist to improve the diversity of the population even if their fitness values are relatively lower.

VI. RESULTS

In this section, the results of the multiobjective optimal sizing and control of the HESS are presented and analyzed in detail. Fig. 8 presented the achieved results when the total mass of the HESS is limited to 320 kg and the average current is used to evaluate the capacity loss. The population size is set to 500 in the NSGA-II optimization algorithm, and the optimization is terminated after about 13 h in a ThinkPad T470P laptop with Intel(R) Core(TM) i5-7300HQ CPU @2.50 GHz CPU and 16GB RAM, which is about five times faster than using

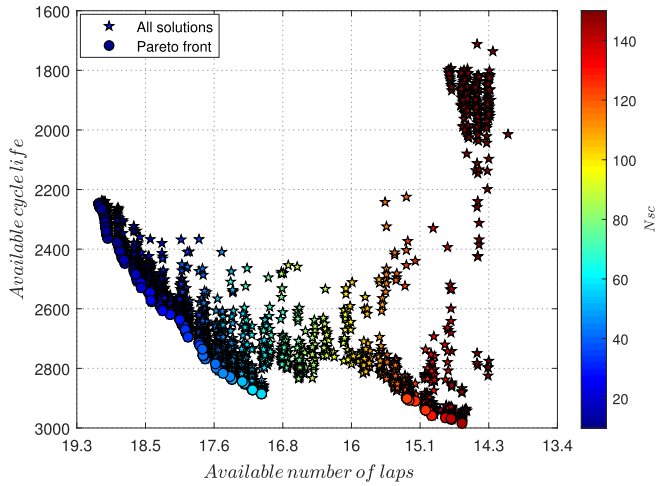

Fig. 9. Pareto solutions using nonuniform C rate when $m_{\text{HESS}} = 320\,\text{kg}$, HESS with 50 SCs can improve the battery cycle life by 27.5%.

a conventional FLC (more than three days) [9]. The number of total iterations is 1839, which means that about 0.92 million solutions have been evaluated during the optimization process. All of the solutions demonstrated in Fig. 8 are associated with corresponding design and control parameters.

From the sizing point of view, using a different number of SCs means different compromises between high power density and high energy density. As it is demonstrated in Fig. 8, utilizing more SCs can assist to reduce the average current of the lithium-ion battery, which is beneficial for longer cycle life of the battery, but reduce the energy density of the HESS, which results in shorter driving mileage. When fewer SCs are used, the results will be the opposite. It is also observed in Fig. 8 that HESS with the same design solutions (makers filled with the same color) may achieve different values of both objective functions, which means that for the same HESS with uniform fuzzy rules, the parameters of the MFs will determine whether we can achieve the Pareto optimal solutions. Thanks to the proposed bilevel optimal sizing and control framework, the corresponding sizing parameter N_{sc} of each HESS and the MF parameters $\mathbf{x}_{\text{mf}}$ of the related EMS are coupled and obtained at the same time for all the solutions including those on the Pareto front.

From Fig. 9, we can see that, when utilize the statistical method to estimate the effect of nonuniform current rate on battery cycle life, the battery cycle life is between 1717 and 2984. The improvements of the available battery cycle life by optimizing the MFs of the FLC based EMS have been further demonstrated in detail in Fig. 10.

Moreover, this article has investigated the optimal sizing and control problems of HESSs with different mass limits. From Fig. 11, we can draw the following basic conclusions. First, HESSs with smaller total mass will cover a fewer number of available laps, but the available cycle life of the battery is longer due to their shorter operating mileage. Second we can achieve a pretty decent compromised solution that can enhance both objective functions with only about 40 SC banks and the optimized MFs.

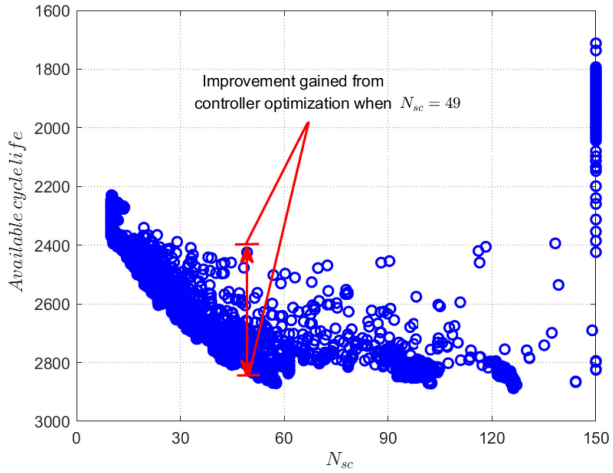

Fig. 10. Battery cycle life improvement by optimizing the FLC-based EMS, the gained improvement of the battery cycle life from controller optimization when $N_{\text{sc}} = 49$ is 15.1%.

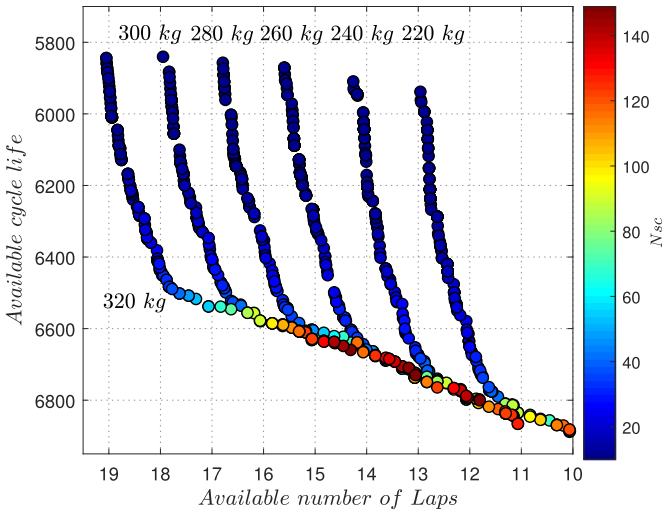

Fig. 11. Pareto optimal solutions for HESS with different mass limits.

One solution from the Pareto front in Fig. 8 ($N_{\text{sc}} = 32$) is selected and compared with the solution with the same sizing parameter but the initially devised MFs. Fig. 12 demonstrates the initial and optimized MFs with the dotted lines and solid lines, respectively.

The achieved available number of laps of the initial and optimized solutions are very similar, which are, respectively, 17.88 and 17.98. This is mostly due to the fact that the two cases are implemented with the same HESS and the available mileage is mainly determined by the sizing parameters rather than the control parameters. However, the available cycle life of the battery is different which are, respectively, 6082 and 6463. This means that HESS with the optimized MFs improved the battery cycle life by 6.3%. Fig. 13 presents the interested variables between 0 and 200 s, as it is illustrated in Fig. 13(a) and (b), the EMS with initially devised MFs tends to request more high peak power from the battery and less from the SCs, which will accelerate the degradation of the battery. This phenomenon can be explained with the curve of SOE in Fig. 13(c). We can

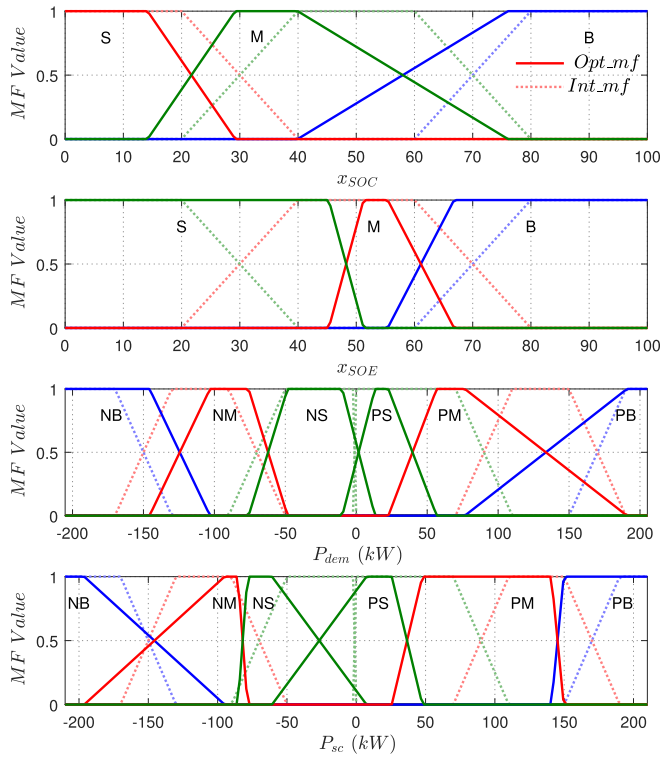

Fig. 12. Initial and optimized MFs when $N_{\text{sc}} = 32$.

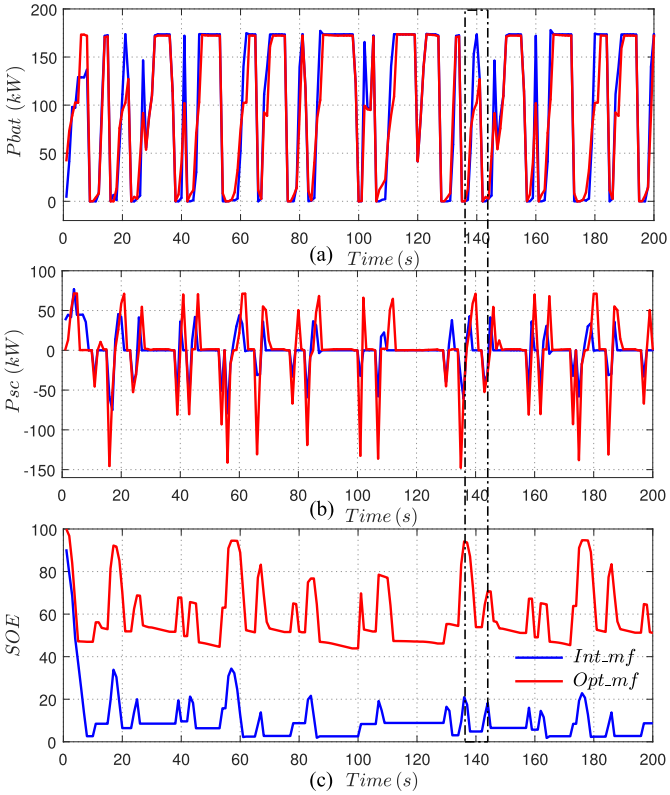

Fig. 13. Pareto optimal solutions for HESS with different MFs, the requested power from the battery is less after optimizing the MFs and the SOE is maintained at a relatively high level due to the optimized EMS.

see that EMS with the initially devised MFs tends to exhaust the SCs very fast at a few seconds after starting the operation and the average *SOE* is under 20% during the simulation which is not capable to provide long-time high peak power to protect the battery. While EMS with the optimized MFs tends to maintain the *SOE* of the SCs above 50%, which helps to play the role of shaving the peak and filling the valley very well during the whole driving profile.

VII. Conclusion

More SCs do not always guarantee a better overall performance, especially when the total mass of the HESS is limited since the energy density of the SC is quite poor and it can be exhausted very fast even if it has high power density. However, we can obtain a balanced performance with fewer SCs and the optimized power management system by the proposed optimization framework. The proposed bilevel optimal sizing and control framework in this article makes it possible to obtain the solutions with enhanced optimality, since it enables the optimization algorithm to search both the design and control parameters simultaneously. The user could choose the favored sizing solution from the obtained Pareto front packaged with the optimal MFs based on a preferred compromise between the two objectives. The obtained global optimal sizing parameters and optimal parameters of the real-time controller on the Pareto front can be put into real-time implementations. In addition to the bilevel optimal sizing and control framework, the devised VFIS with standard interfaces can be used in other kinds of real-time feedback control problems, in particular, it can assist to dramatically improve the computational efficiency when needs to optimize the parameters of fuzzy logic controller.

References

[1] X. Hu, L. Johannesson, N. Murgovski, and B. Egardt, "Longevity-conscious dimensioning and power management of the hybrid energy storage system in a fuel cell hybrid electric bus," *Appl. Energy*, vol. 137, pp. 913–924, 2015.

[2] X. Hu, F. Feng, K. Liu, L. Zhang, J. Xie, and B. Liu, "State estimation for advanced battery management: Key challenges and future trends," *Renew. Sustain. Energy Rev.*, vol. 114, 2019, Art. no. 109334.

[3] G. Suri and S. Onori, "A control-oriented cycle-life model for hybrid electric vehicle lithium-ion batteries," *Energy*, vol. 96, pp. 644–653, 2016.

[4] X. Hu, H. Yuan, C. Zou, Z. Li, and L. Zhang, "Co-Estimation of state of charge and state of health for lithium-ion batteries based on fractional-order calculus," *IEEE Trans. Veh. Technol.*, vol. 67, no. 11, pp. 10 319–10 329, Nov. 2018.

[5] L. Zhang, X. Hu, Z. Wang, F. Sun, and D. G. Dorrell, "A review of supercapacitor modeling, estimation, and applications: A control/management perspective," *Renew. Sustain Energy Rev.*, vol. 81, pp. 1868–1878, 2018.

[6] J. Cao and A. Emadi, "A new battery/ultracapacitor hybrid energy storage system for electric, hybrid, and plug-in hybrid electric vehicles," *IEEE Trans. Power Electron.*, vol. 27, no. 1, pp. 122–132, Jan. 2012.

[7] J. Fang, Y. Tang, H. Li, and X. Li, "A Battery/ultracapacitor hybrid energy storage system for implementing the power management of virtual synchronous generators," *IEEE Trans. Power Electron.*, vol. 33, no. 4, pp. 2820–2824, Apr. 2018.

[8] C. G. Hochgraf, J. K. Basco, T. P. Bohn, and I. Bloom, "Effect of ultracapacitor-modified PHEV protocol on performance degradation in lithium-ion cells," *J. Power Sour.*, vol. 246, pp. 965–969, 2014.

[9] H. Yu, D. Tarsitano, X. Hu, and F. Cheli, "Real time energy management strategy for a fast charging electric urban bus powered by hybrid energy storage system," *Energy*, vol. 112, pp. 322–331, 2016.

[10] J. Shen, S. Dusmez, and A. Khaligh, "Optimization of sizing and battery cycle life in battery/ultracapacitor hybrid energy storage systems for electric vehicle applications," *IEEE Trans. Ind. Informat.*, vol. 10, no. 4, pp. 2112–2121, Nov. 2014.

[11] M. Shahverdi, M. S. Mazzola, Q. Grice, and M. Doude, "Pareto front of energy storage size and series HEV fuel economy using bandwidth-based control strategy," *IEEE Trans. Transp. Electrif.*, vol. 2, no. 1, pp. 36–51, Mar. 2016.

[12] Z. Song, J. Li, X. Han, L. Xu, L. Lu, M. Ouyang, and H. Hofmann, "Multi-objective optimization of a semi-active battery/supercapacitor energy storage system for electric vehicles," *Appl. Energy*, vol. 135, pp. 212–224, 2014.

[13] L. Zhang, X. Hu, Z. Wang, F. Sun, J. Deng, and D. G. Dorrell, "Multiobjective optimal sizing of hybrid energy storage system for electric vehicles," *IEEE Trans. Veh. Technol.*, vol. 67, no. 2, pp. 1027–1035, Feb. 2018.

[14] X. Hu, N. Murgovski, L. M. Johannesson, and B. Egardt, "Optimal Dimensioning and power management of a fuel cell/battery hybrid bus via convex programming," *IEEE/ASME Trans. Mechatronics*, vol. 20, no. 1, pp. 457–468, Feb. 2015.

[15] S. F. Tie and C. W. Tan, "A review of energy sources and energy management system in electric vehicles," *Renew. Sustain Energy Rev.*, vol. 20, pp. 82–102, 2013.

[16] S. Dusmez and A. Khaligh, "A supervisory power splitting approach for a new ultracapacitor battery vehicle deploying two propulsion machines," *IEEE Trans. Ind. Informat.*, vol. 10, no. 3, pp. 1960–1971, Aug. 2014.

[17] Q. Zhang and G. Li, "Experimental study on a semi-active battery-supercapacitor hybrid energy storage system for electric vehicle application," *IEEE Trans. Power Electron.*, vol. 35, no. 1, pp. 1014–1021, Jan. 2020.

[18] S. Hu, Z. Liang, D. Fan, and X. He, "Hybrid ultracapacitor-battery energy storage system based on quasi-Z-source Topology and enhanced frequency dividing coordinated control for EV," *IEEE Trans. Power Electron.*, vol. 31, no. 11, pp. 7598–7610, Nov. 2016.

[19] J. M. Blanes, R. Gutierrez, A. Garrigos, J. L. Lizan, and J. M. Cuadrado, "Electric vehicle battery life extension using ultracapacitors and an FPGA controlled interleaved buck–boost converter," *IEEE Trans. Power Electron.*, vol. 28, no. 12, pp. 5940–5948, 2013.

[20] O. Veneri, C. Capasso, and S. Patalano, "Experimental investigation into the effectiveness of a super-capacitor based hybrid energy storage system for urban commercial vehicles," *Appl. Energy*, vol. 227, pp. 312–323, 2018.

[21] H. Yin, C. Zhao, M. Li, and C. Ma, "Utility function-based real-time control of a battery ultracapacitor hybrid energy system," *IEEE Trans. on Ind. Informat.*, vol. 11, no. 1, pp. 220–231, Feb. 2015.

[22] J. Shen and A. Khaligh, "Design and real-time controller implementation for a battery-ultracapacitor hybrid energy storage system," *IEEE Trans. Ind. Informat.*, vol. 12, no. 5, pp. 1910–1918, Oct. 2016.

[23] O. Laldin, M. Moshirvaziri, and O. Trescases, "Predictive algorithm for optimizing power flow in hybrid ultracapacitor/battery storage systems for light electric vehicles," *IEEE Trans. Power Electron.*, vol. 28, no. 8, pp. 3882–3895, Aug. 2013.

[24] L. Wang, Y. Wang, C. Liu, D. Yang, and Z. Chen, "A power distribution strategy for hybrid energy storage system using adaptive model predictive control," *IEEE Trans. Power Electron.*, vol. 35, no. 6, pp. 5897–5906, Jun. 2020.

[25] B. Hredzak, V. G. Agelidis, and G. Demetriades, "Application of explicit model predictive control to a hybrid battery-ultracapacitor power source," *J. Power Sour.*, vol. 277, pp. 84–94, 2015.

[26] Q. Zhang, W. Deng, and G. Li, "Stochastic control of predictive power management for battery/supercapacitor hybrid energy storage systems of electric vehicles," *IEEE Trans. Ind. Informat.*, vol. 14, no. 7, pp. 3023–3030, Jul. 2018.

[27] M. Wieczorek and M. Lewandowski, "A mathematical representation of an energy management strategy for hybrid energy storage system in electric vehicle and real time optimization using a genetic algorithm," *Appl. Energy*, vol. 192, pp. 222–233, 2017.

[28] R. de Castro, C. Pinto, R. E. Araujo, P. Melo, and D. Freitas, "Optimal sizing and energy management of hybrid storage systems," in *Proc. IEEE Vehicle Power Propul. Conf.*, Oct. 2012, pp. 321–326.

[29] R. E. Araujo, R. de Castro, C. Pinto, P. Melo, and D. Freitas, "Combined sizing and energy management in EVs with batteries and supercapacitors," *IEEE Trans. Veh. Technol.*, vol. 63, no. 7, pp. 3062–3076, Sep. 2014.

[30] Z. Song, X. Zhang, J. Li, H. Hofmann, M. Ouyang, and J. Du, "Component sizing optimization of plug-in hybrid electric vehicles with the hybrid energy storage system," *Energy*, vol. 144, pp. 393–403, 2018.
[31] H. H. Eldeeb, A. T. Elsayed, C. R. Lashway, and O. Mohammed, "Hybrid energy storage sizing and power splitting optimization for plug-in electric vehicles," *IEEE Trans. Ind. Appl.*, vol. 55, no. 3, pp. 2252–2262, May./Jun. 2019.
[32] C. Y. Li and G. P. Liu, "Optimal fuzzy power control and management of fuel cell/battery hybrid vehicles," *J. Power Sour.*, vol. 192, no. 2, pp. 525–533, 2009.
[33] H. Yu and D. Cao, "Multi-objective optimal sizing and real-time control of hybrid energy storage systems for electric vehicles," in *IEEE Intell. Veh. Symp.*, Jun. 2018, pp. 191–196.
[34] X. Hu, Y. Li, C. Lv, and Y. Liu, "Optimal energy management and sizing of a dual motor-driven electric powertrain," *IEEE Trans. Power Electron.*, vol. 34, no. 8, pp. 7489–7501, Aug. 2019.
[35] T. Liu, X. Tang, H. Wang, H. Yu, and X. Hu, "Adaptive hierarchical energy management design for a plug-in hybrid electric vehicle," *IEEE Trans. Veh. Technol.*, vol. 68, no. 12, pp. 11 513–11 522, Dec. 2019.
[36] O. Tremblay, L.-A. Dessaint, and A.-I. Dekkiche, "A generic battery model for the dynamic simulation of hybrid electric vehicles," in *IEEE Veh. Power Propulsion Conf.*, Sep. 2007, pp. 284–289.
[37] P. P. Mishra *et al.*, "Analysis of degradation in residential battery energy storage systems for rate-based use-cases," *Appl. Energy*, vol. 264, 2020, Art. no. 114632.
[38] J. Wang *et al.*, "Cycle-life model for graphite-LiFePO4 cells," *J. Power Sour.*, vol. 196, no. 8, pp. 3942–3948, 2011.
[39] R. Wang, Y. Chen, D. Feng, X. Huang, and J. Wang, "Development and performance characterization of an electric ground vehicle with independently actuated in-wheel motors," *J. Power Sour.*, vol. 196, no. 8, pp. 3962–3971, 2011.
[40] J. Shen, A. Hasanzadeh, and A. Khaligh, "Optimal power split and sizing of hybrid energy storage system for electric vehicles," in *Proc. IEEE Transp. Electrif. Conf. Expo.*, Jun 2014, pp. 1–6.
[41] L. A. Zadeh, "Fuzzy sets," *Inform. Control*, vol. 8, no. 3, pp. 338–353, 1965.
[42] S. Ebbesen, P. Elbert, and L. Guzzella, "Battery state-of-health perceptive energy management for hybrid electric vehicles," *IEEE Trans. Veh. Technol.*, vol. 61, no. 7, pp. 2893–2900, Sep. 2012.
[43] K. Deb, "Multi-objective optimisation using evolutionary algorithms: An introduction," in *Multi-Objective Evolutionary Optimisation for Product Design and Manufacturing*. London, U.K.: Springer, 2011, pp. 3–34.

Huilong Yu (Member, IEEE) received the M.Sc. degree from Beijing Institute of Technology, Beijing, China in 2013, and the Ph.D. degree from the Politecnico di Milano, Milano, Italy, in 2017, both in mechanical engineering.

He is currently a Research Fellow of advanced vehicle engineering with the University of Waterloo, Waterloo, CA, USA. His research interests include vehicle dynamics, optimal control, closed loop control, and energy management problems of conventional, electric, hybrid electric, and autonomous vehicles.

Francesco Castelli-Dezza (Member, IEEE) received the M.Sc. and Ph.D. degrees in electrical engineering from the Politecnico di Milano, Milan, Italy, in 1986 and 1990, respectively.

He is currently a Full Professor with the Department of Mechanical Engineering, Politecnico di Milano. His research interests include studies on dynamic behavior of electrical machines, electrical drives control and design, and power electronics for energy flow management.

Prof. Castelli-Dezza is a member of the IEEE Power Electronics Society.

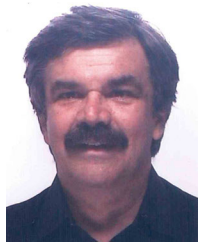

Federico Cheli (Member, IEEE) received the bachelor's degree in mechanical engineering from the Politecnico di Milano, Milan, Italy, in 1981.

He is currently a Full Professor with the Department of Mechanics, Politecnico di Milano, Italy, where, he was an Associate Professor with the Faculty of Industrial Engineering from 1992 to 2000. He is the Co-founder with the E_CO spin-off and an author of more than 380 publications in international journals or presented at international conferences. His scientific activity concerns research on vehicle performance, handling and comfort problems, active control, ADAS, electric and autonomous vehicles.

Prof. Cheli is a member of the Editorial Board of the *International Journal of Vehicle Performance* and *Vehicle Systems Modeling and Testing*.

Xiaolin Tang (Member, IEEE) received the B.S. degree in mechanical engineering and the M.S. degree in vehicle engineering from Chongqing University, Chongqing, China, in 2006 and 2009, respectively, and the Ph.D. degree in mechanical engineering from Shanghai Jiao Tong University, Shanghai, China, in 2015.

He is currently an Associate Professor with the State Key Laboratory of Mechanical Transmissions and with the Department of Automotive Engineering, Chongqing University, Chongqing, China. His research focuses on hybrid electric vehicles (HEVS), vehicle dynamics, noise and vibration, and transmission control.

Xiaosong Hu (Senior Member, IEEE) received the Ph.D. degree in automotive engineering from the Beijing Institute of Technology, Beijing, China, in 2012.

From 2010 to 2012, he did scientific research and completed the Ph.D. dissertation in Automotive Research Center at the University of Michigan, Ann Arbor, MI, USA. He is currently a Professor with the State Key Laboratory of Mechanical Transmissions and with the Department of Automotive Engineering, Chongqing University, Chongqing, China. He was a Postdoctoral Researcher with the Department of Civil and Environmental Engineering, University of California, Berkeley, CA, USA, from 2014 to 2015, as well as at the Swedish Hybrid Vehicle Center and the Department of Signals and Systems, Chalmers University of Technology, Gothenburg, Sweden, from 2012 to 2014. He was also a Visiting Postdoctoral Researcher with the Institute for Dynamic Systems and Control, Swiss Federal Institute of Technology (ETH), Zurich, Switzerland, in 2014. His research interests include modeling and control of alternative powertrains and ESS.

Dr. Hu was the recipient of several prestigious awards/honors, including Emerging Sustainability Leaders Award in 2016, EU Marie Currie Fellowship in 2015, ASME DSCD Energy Systems Best Paper Award in 2015, and Beijing Best Ph.D. Dissertation Award in 2013.

Xianke Lin received the B.S. degree from Zhejiang University, Hangzhou, China, in 2009, and the Ph.D. degree in mechanical engineering from the University of Michigan, Ann Arbor, MI, USA, in 2014.

He has extensive industrial experience with Fiat Chrysler Automobiles, Mercedes-Benz R&D North America, and General Motor of Canada. He is currently an Assistant Professor with the Department of Automotive, Mechanical and Manufacturing Engineering, University of Ontario Institute of Technology, Oshawa, ON, Canada. His research interests include hybrid powertrain design and control strategy optimization, multiscale/multiphysics modeling and optimization of ESS.